JOM, Vol. 74, No. 2, 2022
https://doi.org/10.1007/s11837-021-05034-w
© 2021 The Minerals, Metals & Materials Society

Scale-Dependent Structure–Property Correlations of Precipitation-Hardened Aluminum Alloys: A Review

HUMAIRA ZAFAR,[1,4] MUNA KHUSHAIM,[2,3,5] FLORENT RAVAUX,[1,6] and DALAVER H. ANJUM [1,7]

1.—Department of Physics, Khalifa University, P. O. Box 127788 Abu Dhabi, Abu Dhabi, UAE. 2.—Department of Physics, Faculty of Science, Taibah University, Al-Madina, Saudi Arabia. 3.—Nanotechnology Center, Taibah University, Al-Madina, Saudi Arabia. 4.—e-mail: humaira.zafar@ku.ac.ae. 5.—e-mail: muna.khushaim@kaust.edu.sa. 6.—e-mail: florent.ravaux@ku.ac.ae. 7.—e-mail: dalaver.anjum@ku.ac.ae

Precipitate-hardened aluminum (Al) alloys are being actively developed to further improve their fundamental mechanical properties, namely Young's modulus (Y_m), and strains for both existing and future applications. Their development critically depends upon figuring out the structure–property correlations (SPCs) between the microstructure and the mechanical properties. Various techniques can be used to establish SPCs between the determined microstructure and the observed mechanical properties of the alloys. In this paper, we review techniques that allow the measuring of the alloy properties under both "direct" and "in-direct" categories. In the former, the properties are measured by applying loads, while for the latter case, they are measured without applying loads. However, for both categories, the regions of the determined structure are directly related to the same regions where the properties are measured. It was found that the validity of the established SPCs depends on the length scales, and that often a combination of techniques is required to complete the task.

INTRODUCTION

Metals including aluminum and iron are in abundance on earth,[1] and therefore their use is found to be ubiquitous in our daily lives.[2,3] The metal industry is an ever-expanding business which demands high strength, lighter weight, and increased efficiency. With additional requirements of being corrosion-resistant and environment friendly, aluminum (Al) metal alloys have come to light as one of the most important materials for the automobile chassis and space-craft industry. Although Al alloys cannot compete with the high strength of structural steel (400 MPa), they rule in terms of a higher strength-to-weight ratio (Al is about half the weight of steel), making it an excellent choice for applications where a lightweight material is highly desirable. Moreover, Al alloys also exhibit high corrosion resistance through the effect of passivation, and therefore have several applications in the field of corrosion-resistant materials. The most frequently used Al alloys are Al-Cu (2xxx), Al-Mg-Si (6xxx), and Al-Mg-Zn (7xxx), with other elements added as precipitates to enhance their mechanical properties. These precipitates exhibit diverse morphologies, demanding complete characterization techniques in terms of their atomic configuration. Remarkable efforts in Al alloy research and development involve the characterization of microstructural features and varying compositions at the nanoscale, using microscopy techniques to understand structure–property correlations (SPCs).

The transportation industries constantly strive to achieve minimum weights to cut fuel consumption and to improve overall performance. Different innovative design strategies have been placed and directed toward weight reduction, combined with retaining or enhancing the mechanical behavior. In this context, Al-based alloys play a key role in

(Received July 21, 2021; accepted November 8, 2021; published online January 13, 2022)

modern engineering and are widely used because of their light weight and superior mechanical properties. They have been widely used in automotive, aerospace, and construction engineering due to their good corrosion resistance, superior mechanical properties, superior machinability, easy weldability and relatively low cost.[4,5] The progress in practical applications has been determined by the intensive research and developmental work on such alloys. For the past several decades, Al alloys have been the primary material choice for structural components of aircraft and automobiles. Well-known performance characteristics, known fabrication costs, design experience, and established manufacturing methods are the reasons for the continued confidence in Al alloys, ensuring their use in significant quantities for the rest of this century.[6] However, in the early years, Al alloys were developed by trial and error. For the time being, the improvement of Al-based alloy has been performed based on the understanding of the relationships among compositions, processing, microstructural characteristics, and properties.

Metal alloys can be synthesized to have certain properties superior to original metals by selecting proper alloying elements, and processing method during their mixing with host metals. For instance, Al–Li alloys are lighter and have high tensile and yield strength compared to the conventional high-strength aluminum alloys. But these alloys possess low toughness and poor ductility as mentioned. When Al is alloyed with lithium, for every 1 wt.% addition of lithium (Li), there is an approximately 3% reduction in alloy density and an increase in stiffness of approximately 6%.[7] On the downside, Al-Li alloys suffer from low toughness, poor ductility, and poor weldability,[8] which make these alloys an unattractive material for engineering applications. To overcome these difficulties, various modifications in alloy chemistry and fabricating techniques have been used to improve ductility while maintaining high strength. Copper (Cu), magnesium (Mg) and zirconium (Zr) solute additions have been shown to have beneficial effects.[8] Mg and Cu improve the strength of Al-Li alloys through solid solution and precipitate strengthening, and can minimize the formation of precipitation-free zones near grain boundaries.[9] In the context of customizing the material properties to very specific applications, a series of high-strength Al-Li-Cu alloys containing minor additions of Mg, silver (Ag), and Zr, called Weldalite, have been developed. This series of alloys shows good characteristics of density and modulus with damage tolerance and corrosion properties to equivalent formerly used materials.[10] Moreover, the Weldalite family exhibits significant strength–toughness combinations upon application of heat treatment.[11]

The relationship between the fundamental mechanical properties (Young's modulus) and the microstructure of Al alloys depends strongly upon their elemental composition, and their thermal processing. The thermal processing includes several parameters, such as aging temperature, annealing time, storage time at room temperature, and heating/cooling rates. Generally, the microstructure of the Al-Li-Cu system consists of a number of phases, the most important being the T_1Al_2LiCu phase. However, depending on the alloy composition and processing conditions, other minor phases can be precipitated, such as $\theta'(Al_2Cu)$, $\delta'(Al_3Li)$ and $\beta'(Al_3Zr)$ phases. The addition of minor elements can result in a diversity of precipitates. For example, the addition of Mg to the $Al-Cu-Li$ alloy promotes the formation of phases in the $Al-Cu-Mg$ system. In Al alloy, as a class important engineering material, subtle variations in chemistry can strongly influence the decomposition of the supersaturated solid solution and hence result in the development of different precipitate phases, as shown in Figs. 2 and 3. Numerous important advancements have already been made on establishing the SPCs for Al alloys by applying microscopy-based techniques. For instance, nano-indentation experiments of metal alloys in transmission electron microscopy (TEM) allow the establishment of a dynamic correlation between the evolution of their microstructure and the applied load. With the application of such techniques, the entire emphasis of this review in on correlating the acquired image of an area with the mechanical property (e.g., Young's modulus and/or strain) measured from the same area. Granted that the imaging area and mechanical property determinations sometimes require very different techniques, it may become a difficult task to apply both of techniques exactly on the same area. For instance, the imaging is carried out using optical, electron, and scanning probe types of microscopy techniques. While the mechanical properties such as Young's modulus (Y_m) are determined using the nano-indentation (NI) technique which provides information at the spatial resolution of several tens of nanometers. Even though Y_m is a macroscopic mechanical property of materials, it is independent of size in the linear elastic regime. However, at the nanoscale, it has been observed that the behavior of mechanical structures cannot be explained by using macroscopic theory and a constant value of the Y_m. Therefore, the Y_m of nanomaterials changes to Y_{m-eff} which can be larger or smaller than the bulk counterpart. Several factors can contribute to change the Y_m of materials at the nanoscale.[12] The most important and predominant factors are residual stress (RS), couple stress (CS), grain boundaries (GB), surface stress (SS), surface elasticity (SE), and nonlinear (NL). It is to be noted that all of these factors may or may not be affecting Y_m at the nanoscale for a given materials system. Generally, it is either two or three of these factors that are at play for a given nanomaterial. This is why it is

important to determine Y_{m-eff} in the vicinity of precipitate/Al matrix interface. For isotropic and homogeneous materials, elastic moduli are independent of their position within the solids. Therefore, in the linearly elastic regime, they are reduced to the special form of Hooke's law which is represented by the equation:

$$\sigma = Y_m \varepsilon \tag{1}$$

This equation implies that the applied stress distribution in the materials depends upon the strain, but it scales with Y_m. The Y_m is usually a constant in Hooke's law at bulk scales. However, as stated above, it can change at the nanoscale, and thus the yield strength of nano-precipitates may differ from the values predicated by Hooke's law. In this way, the determined distribution of stresses will not represent the actual situation. Therefore, as a solution to this issue, both Y_m and ε should be determined experimentally by using independent techniques to obtain an accurate stress map. Generally, σ and ε are vectors and Y_m is a scalar quantity in the equation.

This paper reviews the techniques that allow correlating, in the macro- to nano-range of lengths, the microstructure (S) of the Al alloys with their fundamental mechanical properties (P) as given in the equation. These properties are Y_m and ε and only those techniques are included that allow establishing a direct correlation between the measured properties and the microstructure. The direct correlations or established SPCs represent situations in which the imaging of the microstructure and the property measurements are carried out on the same areas of the samples. A schematic showing the sought SPCs is given in Fig. 1.

The presented schematic is quite general and implies that several experimental techniques will be required to establish a direct correlation between the microstructure and the mechanical property of the alloys. Further, there will no single technique to image the microstructure and measure the property that will work in the entire range of macro- to micro-scales. In fact, it will be seen from the proceeding sections that different techniques will also be required to image the microstructure. In this review, the emphasis is only on the fundamental mechanical properties, namely Young's modulus and strains. Broadly speaking, the mechanical property measuring techniques are divided into two main categories, namely direct and indirect. For the case of the direct category, a load (or σ) is applied to generate tensile strain ε_T. This way, the ratio of applied stress and measured strain give rise Y_m in the linear elastic regime, whereas, for the case of the indirect category, the residual stresses (σ_R) are measured by determining the Y_m and residual ϵ_R. The spatial resolution, sensitivity, and applicable range of each applied technique is discussed here at length. For example, NI is the only direct

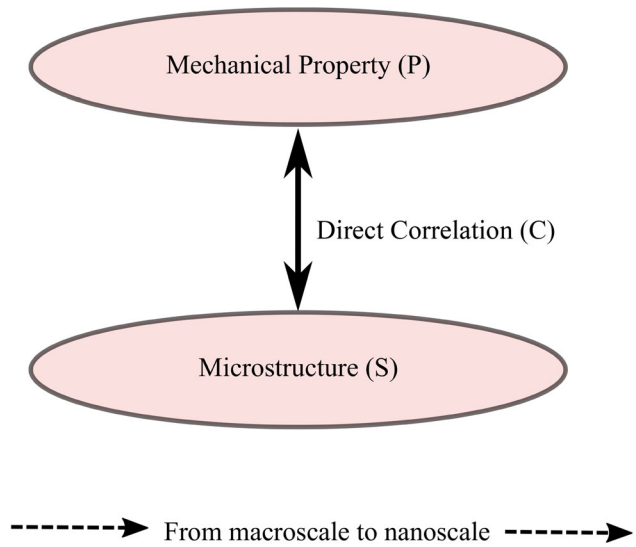

Fig. 1. Schematic of a method for directly correlating the microstructure with the mechanical properties of Al alloys. Different imaging techniques, and likewise mechanical property measurement techniques, are required to image the microstructure, and to determine the mechanical property of the alloys at different spatial resolutions, respectively.

category technique which allows the determining of both ε and Y_m. Similarly, nanobeam electron diffraction (NBD) combined with electron energy loss spectroscopy (EELS) are the only indirect category techniques that allow the determining of both ε and Y_m simultaneously. All other techniques provide either ε or Y_m but not both. The details and the characteristics of these techniques are discussed in the following sections. First, the details that provide information at bulk scale are presented and then the techniques that work at the nanoscale are presented. In the end, the future outlook of this field is discussed by looking at the latest developments which have occurred recently in both fields of electron microscopy and atom probe tomography (APT) such as four-dimensional scanning TEM (4DSTEM).

The local elemental composition of the alloys dictates their microstructure and mechanical properties. Therefore, the control of compositions or phases of the precipitates is central to achieving the desired mechanical properties of the alloys. That is why, for the sake of completeness, the role of composition in the Al alloys has been discussed here before talking about the SPCs. In a historical sense, the composition of the precipitates had been found indirectly by determining the phases of the precipitates by using diffraction-based methods of conventional TEM techniques, namely dark-field TEM and bright-field TEM. These methods not only provide the information on the phases of the precipitates but also enable the determining of their orientations with respect to a particular grain orientation of the host metal. In spite of the success of these methods, currently, it is a desirable thing to

simultaneously visualize the orientation of the precipitates along with their elemental composition at atomic scales. This is typically achieved by using the advanced techniques such as APT and aberration corrected scanning TEM (STEM) in conjunction with energy-dispersive x-ray spectroscopy (EDS). In this context, APT provides one of the most spectacular microscopic information on existence of precipitates in the alloys by giving a three-dimensional (3D) image at the atomic scale with single-atom sensitivity. Moreover, each atom or isotope in the image can also be identified as well. The fundamental data format is the 3D position and identity of individual atoms in a volume that contains potentially millions of atoms; thus, different information about the analyzed material can be extracted. A detailed information about APT can be found elsewhere.[13,14] It is to be noted that atom probe studies have provided a range of information on the different types of precipitates present in Al-Li-Cu alloys. Specifically, the APT analysis of complex Al alloy can reveal the composition and orientation at nanoscale of precipitates in the Al matrix. The typical morphologies of the precipitates exist in small thickness (between 1 and 2 nm) and closely spaced to each other ($\approx$ 9 nm), as can be seen in Fig. 2. It all leads to the approach of an optimal situation which corresponds to the high hardness value (215.5 $\pm$ 8 HV) and, hence, a high level of strengthening would be expected.[15]

That is because the maximum hardening is usually associated by the spacing between particles equal to 10nm.[16] The nominal chemical composition of this alloy is as follows: 4 wt.% Cu, 1 wt.% Li, 0.36 wt.% Mg, 0.28 wt.% Ag, 0.14 wt.% Zr, and 94.22 wt.% Al. The maximum hardening occurs due to the presence of the $T_1(Al_2LiCu)$ phase. This type of an optimal situation arises from the presence of the precipitate particles that are not that small to be shared by dislocations and yet are too closely spaced to allow bypassing by dislocations. According to APT analysis in Fig. 2, the increment of the aspect ratio (length to thickness $\approx$ 20-22) causes the formation of a closed network of platelet precipitates which entraps gliding dislocation. This is how the manipulation with second-phase precipitates in the microstructure is an important option to control the mechanical behavior of the complex Al alloy. Applying a plastic deformation prior to artificial aging has been highlighted as an important tool for this manipulation. In summary, it can be stated that APT makes a unique contribution within the field of light Al alloys and can be used for the developments of Al alloys in the future.

Atomic-resolution spectroscopy in the aberration-corrected STEM mode is another way of determining the morphology and composition of the precipitates in Al alloys at nano-scale resolutions. It is becoming a common technique to correlate the composition and structure of precipitates with the host matrix. The atomic-resolution spectroscopy generally involves EELS and EDS. Owing to the fast acquisition and information-rich spectra, EELS is a dominant technique for carrying out the spectroscopy analysis of the Al alloys. It can give information on thickness, oxidation state, chemical bonding, mechanical, and optical properties in addition to elemental composition, whereas EDS only measures the elemental composition and requires exposing a specimen to a vast number of electrons to produce enough signal to extract atomic-resolution information. Wenner[17] has outlined several key characteristics of STEM-EELS and STEM-EDS (80 kV aberration-corrected) mapping techniques on ordered precipitates in aluminum alloys. For instance, first, it allows the carrying out of mapping experiments of thicker specimens ($\approx$ 150 nm) if electron beam broadening and de-channeling is not too severe. Second, the spatial resolution is typically better than with EELS, as very localized (< 1 nm) higher energy peaks are available for elemental mapping.[18] Third, some carbon contamination can

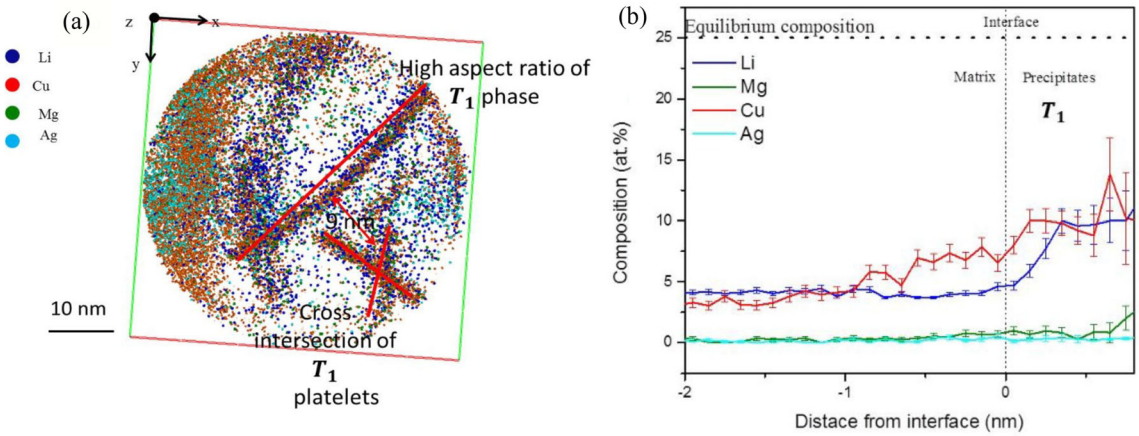

Fig. 2. APT analysis of AA2195 at 1 % deformation level (aged for 10 h at 150 ° C) (a) Top view of the reconstructed volume showing the nice distribution and dimension of the nano-features. (b) Composition profile proxigram of the observed T_1 platelets. Reprinted with permission from Ref. 15.

be tolerated, where it would completely devastate a high-loss EELS spectrum. Four, overlap between different elemental x-ray peaks is rare, and, even in case of overlap, the peaks can be deconvoluted due to their simple Gaussian shape. Five, modern silicon drift detectors have a negligible and Poisson-distributed dark noise, which means that each elemental peak can be straightforwardly integrated but also summed across multiple spectra, with increasing signal-to-noise ratios for longer acquisitions. Six, any dwell time can be used with EDS, while EELS requires some time for spectrum readout, preventing fast multi-frame scanning. STEM-EDS analysis of the Al–Mg–Si–Cu alloy is performed to correlate the composition of precipitates with the phases of the alloys. The performed analysis is given in Fig. 3, showing the summed EDS maps of the Q' phase with no averaging over symmetries. The Q' phase, which is isostructural to the equilibrium Q phase, seems from the symmetry-averaged images to have the composition $Al_6Mg_6Si_7Cu_2$. This fits with the compositional framework found for the Q phase by x-ray diffraction, $AlxMg_{12-x}Si_7Cu_2$ with $x = 6$; or by density functional theory calculations; $Al_3Mg_9Si_7Cu_2(x = 3)$ with $x = 3$. The particle is uniform throughout the image, except for a few unit cells to the left, where a compositional change was observed. In the Q' model in Fig. 3, the two sites labeled A and B are occupied by Al. In the marked areas in the Al map in Fig. 3b, only three out of these six sites are bright. In this part of the precipitate, Al occupies either site A or B within one "ring" of the Al/Mg columns, and transitions between A↔B occupation are evident in neighboring "rings". The remaining three columns are not present in the very clear Si and Cu maps, and should therefore be occupied by Mg. This is consistent with the change to a less bright atomic number contrast in the ADF images, and can be observed as a dark line marked in the overview image (Fig. 3j). Figure 3i also shows the Fourier transform of the Si image in Fig. 3d. In addition to the clear hexagonal structure, a weaker, longer-range periodicity can be discerned. The spots correspond to the lattice parameter of the Q' phase. Copper is left as the only element which has a uniform intensity across all its designated columns.

THE DETERMINATION OF YOUNG'S MODULUS

The Direct Methods

NI is a commonly used and widely accepted technique for determining the hardness and elastic modulus of a wide range of materials.[19] This is because it has several advantages for measuring the mechanical properties, including the minimum preparation for the experiments and because the experiments can be redone several times on the same specimens.[20] It is a contact-based technique and thus the shape of the contacting tip with material during the experiments is very important. A sharp pyramid-shaped diamond with a tip of a few tens of nanometers radius is pressed onto the sample. The applied load and nano-scale displacements in the sample are recorded and the mechanical properties are analyzed from the load–depth curves. Yu and co-workers made experimental observations of a high-speed NI of a rigid pyramid-shaped tip into the Al substrate and explained the acquired results by using molecular dynamics simulations, and the critical indent stress value of the pure Al was estimated to be 6 GPa.[21] They also investigated other mechanisms possibly occurring during the NI experiments, such as local melting, tip substrate bonding, indentation force, and

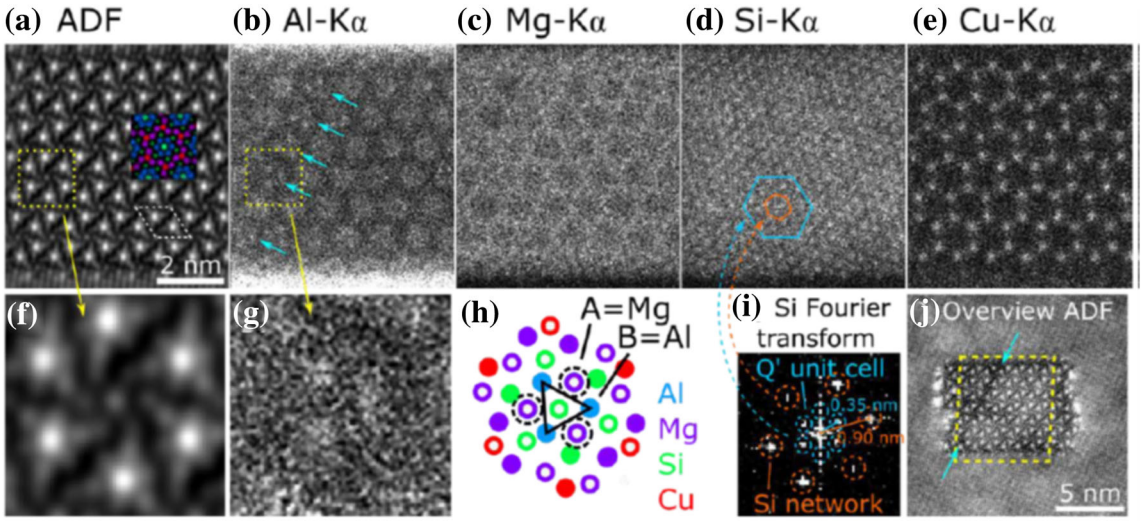

Fig. 3. (a–e) Full aligned and summed ADF and EDS images of the Q' phase in the Al–Mg–Si–Cu alloy. (f–h) Close-ups and model of an example area where the "Al ring" has composition Al_3Mg_3 instead of Al_6. (I) Fourier transform of the Si image. The *inner spots* arise from the intense Si columns at the corners of the Q' unit cell. (j) Overview image taken before the scan, showing a *dark line* where the structure is Mg-rich. The scan area is indicated with a *yellow dashed square*. Reprinted with permission from Ref. 17 (Color figure online).

material orientation. It was noted that higher temperatures and indent forces lead to higher indent depths because the dislocations move easily. The Y_m of the materials to be investigated is generally determined in the reduced form given by Eq. 2.

$$\frac{1}{Y_{m-eff}} = \frac{1 - -v^2}{Y_m} - \frac{1 - -v_i^2}{Y_{m_i}} \tag{2}$$

where Y_{m-eff} is the effective Young's modulus of the material and indenter, Y_{m_i} is of the indenter. v the Poisson's ratios of the material, and v_i is the Poisson's ratios of the cantilever. The applied load as a function of displacement graphs are generated in this way (see Fig. 4). In the model being referenced, the Molecular Dynamics simulation were carried out with the ParaDyn code. A small-time step of 0.001 ps was used, and the atomically sharp tip was moving into contact with a flat Al substrate. The movement is normal to the Al substrate surface. The tip was equilibrated and the substrate for 3 ps at the desired temperature. Then, the tip was placed at 6 above the substrate, so that there is no interaction between the tip and the substrate at the beginning, and a constant force is applied to the top layer of the tip, accelerating it towards the substrate. The typical maximum velocity is 3 ps^{-1}, or 300 ms^{-1}. The slope of the generated enable determining the effective Young's modulus in the equation:

$$Y_{m-eff} = \frac{1}{2\beta}\sqrt{\frac{\pi}{A}}\frac{dP}{dh} \tag{3}$$

where β is the geometrical factor, A is the contact area of the indenter with the sample surface. The various NI techniques have been used to see large variations in the hardness and Young's modulus of Al alloys. In Ref. 22, the quasi-static indentation and the dynamic modulus mapping methods were used to study the complex nanostructure of Al foam cells. The results obtained from several NI approaches were compared, exhibiting consistent values of effective elastic modulus and intrinsic properties of the individual phases. This is because of the appropriate arrangements of the NI experiments (each indentation technique is able to evaluate the mechanical properties at different scales), in terms of correct calibration, indenter type, imprint size, and loading parameters. In Ref. 23, complex intermetallic phases in an Al-Si alloy system were investigated by using the same technique. Hardness and modulus values for a range of alloy compositions were observed in that case. The presented results showed that the NI technique is able to detect the enhancement in the mechanical property with increasing ratio of nickle (Ni) in Al-Cu-Ni phases. Additionally, the authors correlated the enhanced elastic modulus with the high formation temperature of the intermetallic phases. In another test on a nanocrystalline Al-Mg alloy, the

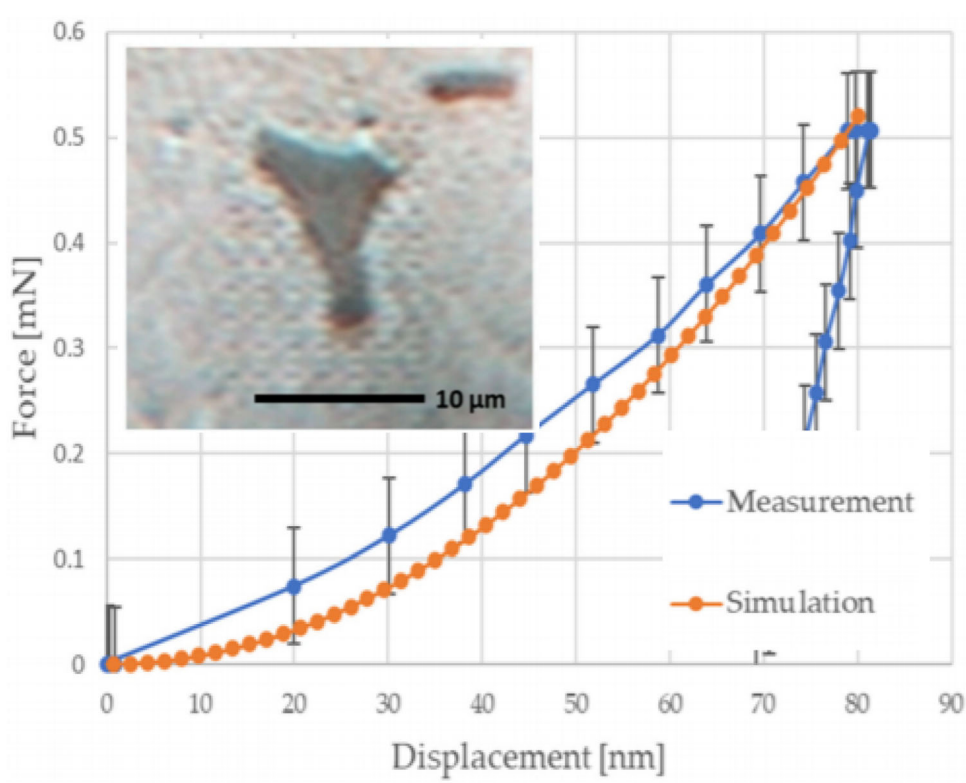

Fig. 4. Typical force versus displacement curves, a comparison of NI curves for experimental measurement and corresponding simulation. Reproduced under the terms of the Creative Commons CC-BY license (http://creativecommons.org/licenses/by/4.0)[30]

acquired data were analyzed by using two different techniques proposed by Dao and co-workers.[24] and Ogasawara and co-workers.[25] The obtained values of elastic modulus, hardness, strain-hardening exponent, and yield stress confirm the applicability of both Dao's and Ogasawara's models.[26] NI is also a useful tool in characterizing the uncertain areas of welded Al alloys as reported in Ref. 27. In this study, the residual stress was measured in two commercially available Al alloys and tension in the weld zone was reported in both the longitudinal and transverse directions. Moreover, NI tests have been commonly used to see the complex morphologies which are hard to test due to their size. The limitations and strengths of the two NI on approaches (constant load test and constant strain rate test) were explored by Shen and co-workers.[28] Mechanical properties of Al alloys are strongly dependent on the elastic and shear moduli of the second phases, which are critical to test in NI as they penetrate the matrix during the test. To circumvent this issue, an efficient approach to test the mechanical characteristics of the second phases was adopted in Ref. 29. The millimeter-scale bulky second phases were prepared through calculation of phase diagrams and directional solidification. Reliable NI and Vickers hardness tests were then performed to determine the elastic moduli and hardness of the α-*AlFeSi*, β-*AlFeSi* and Mg_2Si phases. The spatial resolution of both image and NI area can be dramatically improved by moving nano-indentors inside SEM and/or TEM instruments. Both allow measuring various mechanical properties at the nanoscale in addition to providing the images of corresponding areas at similar resolutions.

In a recent study of intermetallic particles of the 2024 Al alloy, it was observed that the NI test gives different results for a particle with similar mechanical properties depending on its depth in the tested surface, leading to different force versus displacement characteristics. A typical load–displacement curve is shown in Fig. 4.[30] They also obtained hardness and Young's modulus along with the optical microscope images (see inset in Fig. 4) of the examined particle.[30] Although impressions made by NI can be captured using an optical microscope, complex microstructures and strain measurements at the nanoscale can be better observed by using electron microscopy, which allows inspection at the atomic scale, replacing optical microscopes with superior spatial resolution. The load–displacement curves and high-resolution images have been obtained in Ref. 31 using a combination of NI with SEM, as shown in Fig. 5). The images were extracted from an SEM video recorded during the indentation test, and correspond to the letters indicated in the curve. Image (a) corresponds to the initial point of contact; (b) to peak load; (c) to delamination of the film from the substrate; (d) to immediately after the film has released from the diamond; and (e) to just after completion of the test. The most obvious aspect of the studies presented in Fig. 4 is that along with the conventional load–strain data, the optical images of the corresponding areas are also presented. These images allow the establishing of the correlation between the microstructure and the property. Albeit at a low spatial resolution of about 300 nm which is inherently provided by the optical microscopy technique. To further improve the spatial resolutions of both microstructure and Y_m, the NI experiments

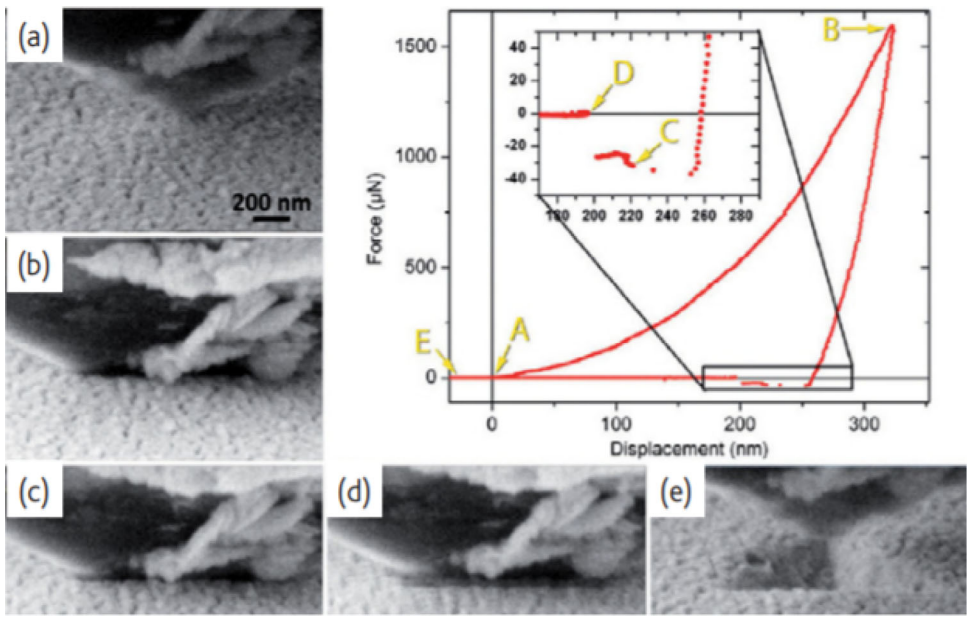

Fig. 5. Force–displacement curve acquired during a displacement-controlled test: (a–e) were extracted from an SEM video recorded during the indentation test and correspond to the *letters* indicated in the *curve*. Reprinted with permission from Ref. 31.

can be carried out in a TEM. In these experiments, the tip size of the indentater can be further reduced to enhance the spatial resolution. TEM enables imaging the microstructure at highest resolution possible. In situ TEM experimental results of measuring the Y_m of Al alloys is shown in Fig. 6. The hardness values were calculated for the Al alloy deformed with different deformation levels of 0 % (non-stretched), 1 %, 2 %, 3 %, 4 % and 5 %. It was noted that the hardness values are somewhat high at the beginning and then decrease followed by increasing to the peak hardness value. At the end of the curve, the hardness values decrease to relatively stable values.[15] The obtained hardness values were in the range of 114 ± 5 HV/1.96 to 215 ± 4 HV/1.96. It can be seen that compression from the indentater leads to the generation of applied load versus displacement plots that lead to the determination of Y_m for the alloys.[32] The strain fields and Young's modulus (Y_m) of the hardening precipitates in Al alloy in $[00-1]_{Al}$ and $[-110]_{Al}$ directions was estimated in the range of ± 0.1 % to ± 0.16 % for the thin and thick T_1 precipitates, 0.2 % to 0.05 % for the β' precipitate, and in the range of 0.01 % to 0.02 % for the Al matrix.[38] The mapping of Y_m in the Al matrix around each type of hardening precipitates within the alloy microstructure yielded the values of 67.41 ± 1.1 GPa, 65.1 ± 1.1 GPa, 70.41 ± 1.1 GPa, and 69.13 ± 1.1 GPa for the Al matrix near the thin T_1 platelet precipitate, thick T_1 platelet precipitate, β' spherical precipitate, and Al matrix, respectively. The hardness evolution during the heat treatment of the alloy for different temper conditions were also estimated.[15] The first feature of interest is that an Al alloy in T8 temper has a higher hardness of 160.3 ± 7 HV/1.96 than those of the specimens in the T4 and T6 tempers. During T4 and T6 tempering, both specimens experience a significant and quite similar hardening response. The minimum hardness value is reached in T6 tempering with value of 112 ± 5 HV/1.96. During the natural aging of the sample in the T4 temper, no significant change of hardness is observed with the value of 125.2 ± 9 HV/1.96. This behavior can be attributed to the presence of different nanoscale structural features after the conducting of each heat treatment temper.

The Indirect Methods

The dynamic measurements such as impulse excitation technique (IET) of the Y_m is an alternative to conventional tensile tests. The strain interval used for the dynamic measurement of Y_m is small, which means in turn that stresses are small enough to ignore dislocation activity, as is the build-up of internal damage. The sample then behaves more truly as a linear elastic solid. Another advantage of this low amplitude method is that particles are kept in compression (due to thermal internal stress upon cooling), and therefore possible cracks in the particles remain closed. For these reasons, the measurement is expected to yield a higher and more accurate value compared to conventional tensile measurements from mechanical tests. Among the dynamic testing methods, the IET consists of subjecting a specimen to an external mechanical impulse and recording its resonant frequencies. Elastic properties can then be computed from these harmonic frequencies, knowing the geometry of the specimen and its density.[33,34] Strictly speaking, these are "dynamic" elastic moduli but,, for the sake of brevity, we will omit the word "dynamic". Practical application of the method has been reported for various composite materials. Y_m is measured by applying the free longitudinal vibration of a beam that engenders longitudinal extension and compression of the beam and some lateral

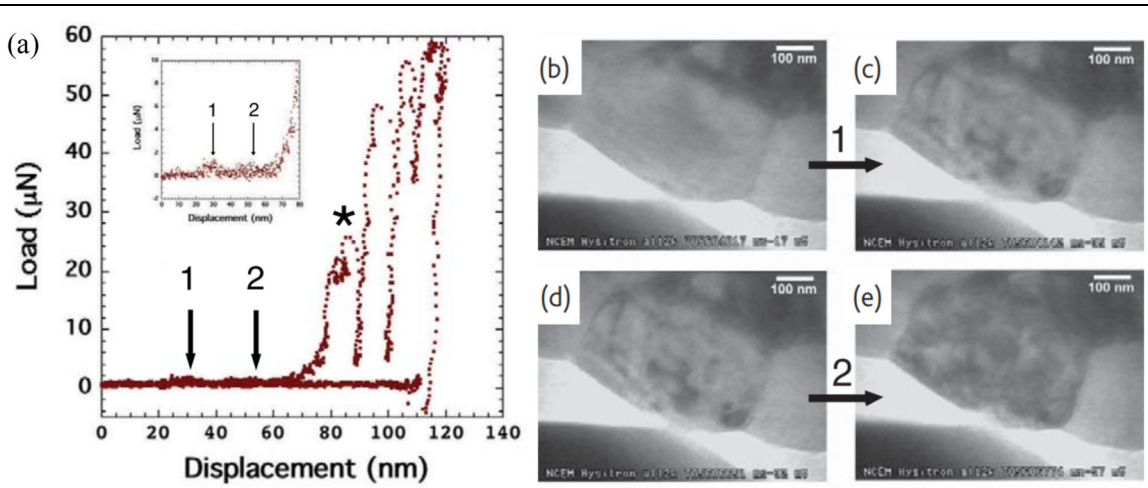

Fig. 6. (a) Depth-controlled load–displacement curve exhibiting several sudden load-drop events as the indenter moves into the Al grain. *Inset* initial portion of the loading segment. *Arrows* point to two barely discernable load transients corresponding to the first two dislocation bursts within the grain. *Star* indicates the start of the first major load-drop event. (b, c) and (d, e) Sequential TEM movie frames from the first and second dislocation bursts, respectively. Reprinted with permission from Ref. 32.

deformation. The latter can be neglected when the bar is long compared to its cross-section. Under the conditions of the first fundamental harmonic (f_1) and geometrical corrections, the Y_m can be determined by using Eq. 4:

$$Y_m = 0.946 {f_1}^2 \rho \frac{l^4}{h^2} \tag{4}$$

where ρ is the density of the material, and l and h are the length and height of the beam, respectively. The task imaging the areas where the IET testing is performed is also carried out using optical microscopy. A typical optical image of an Al alloy and the determined relative Y_m for various alloys are shown in Fig. 7. The IET technique has similar limitations on spatial resolutions when it is combined with optical imaging. That is, the resolution of the acquired images also lies in the range of 300 nm or higher, whereas the spatial resolution for the determination of Y_m lies in the range of a micron or higher.

Spatial resolution of Y_m for the case of "indirect" category can be enhanced by carrying out the IET in the in situ SEM. The setup and data on Al alloys for carrying out the IET experiments as well as the microstructure imaging is presented in Fig. 8. Bartolomé and co-workers[34] measured not only Y_m by applying the IET signal but further utilized it to investigate the crack formation in the alloys. The evolution in the microstructure under IET in in situ SEM is presented in Fig. 8b-e. The amplitude of the oscillating rod as a function of the voltage frequency was measured from the images on the SEM screen. The frequency was tuned to find the resonance of the oscillating rod, and the Young's modulus was then determined from the elasticity theory, as shown by Eq. 5:

$$Y_m = \frac{f_i^2 4\pi^2 L^4 \rho S_B}{I_B \alpha^2} \tag{5}$$

where f_i is the fundamental resonance frequency, L the length of the rod, ρ the density, S_B and I_B are the section and the second moment of inertia at the base of the rods, respectively, and α is the correction factor, which depends on the geometry of the rod.

Despite measuring the strain fields around the precipitates at the nanoscale, the engineering strain–stress curves cannot be utilized without the measurements of the Y_m independently in alloys at the same spatial resolutions. As mentioned earlier, the low-loss EELS technique allows the determining of theY_m values in metal alloys. The combined application of EELS with the dark field STEM mode enable mapping of Y_m at the nanoscale of the same regions of alloys from where the strain fields are determined. The low-loss EELS method relies on the fact that the bulk plasmon energy (E_p) in the acquired EELS of metallic alloys is related to the Y_m of the matrix alloy. The complete theory of correlation between plasmon energy (E_p) and different elastic properties of various alloy materials has been completed, as already demonstrated by using TEM-EELS.[35] As is known, the volume E_p varies with the valance electron density (n) of a material, and hence various equations relating E_p to the bulk modulus (B_m), Y_m and shear modulus (G_m) have been developed.[36,37] The value of Y_m for Al alloys was determined from its E_p by using Eq. 6, showing the relationship between E_p and Y_m:

$$Y_m = 0.08 {E_p}^{2.5} \tag{6}$$

The application of the method galvanizes around the objective of extracting the value of bulk plasmon frequency or energy pixel-by-pixel from the acquired STEM-EELS hyper-detests. Next, the shift in the

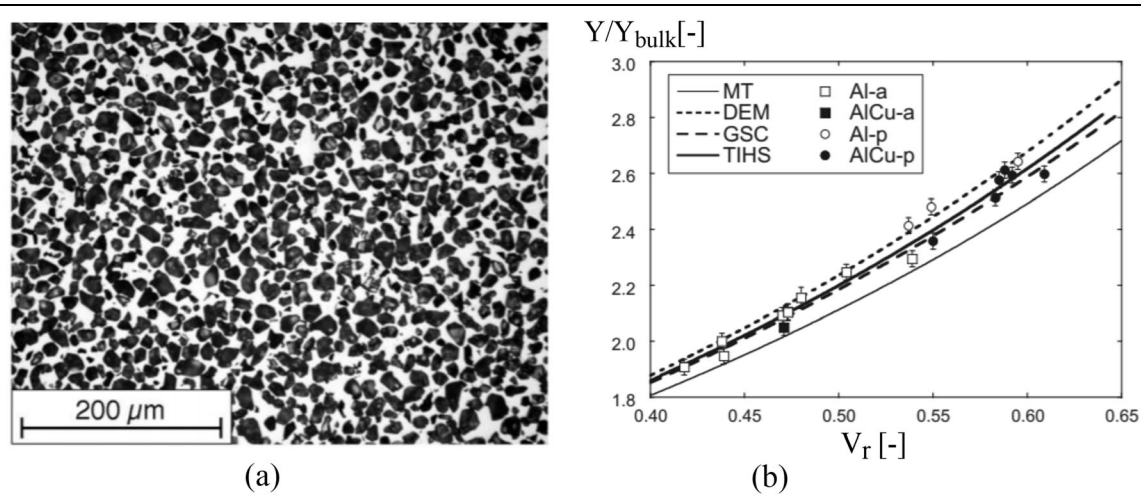

Fig. 7. Measurements of Y_m using an indirect method. (a) Optical micrographs of PRMMCs with a 25μm polygonal. (b) Relative Young's modulus measured by IET (calculated according to DIN 1048) and compared with analytical models. Different types of composite are referred to with different symbols: Al an Al matrix, AlCu an Al–Cu alloyed matrix, a and p angular and polygonal particles, respectively. Reprinted with permission from Ref. 33.

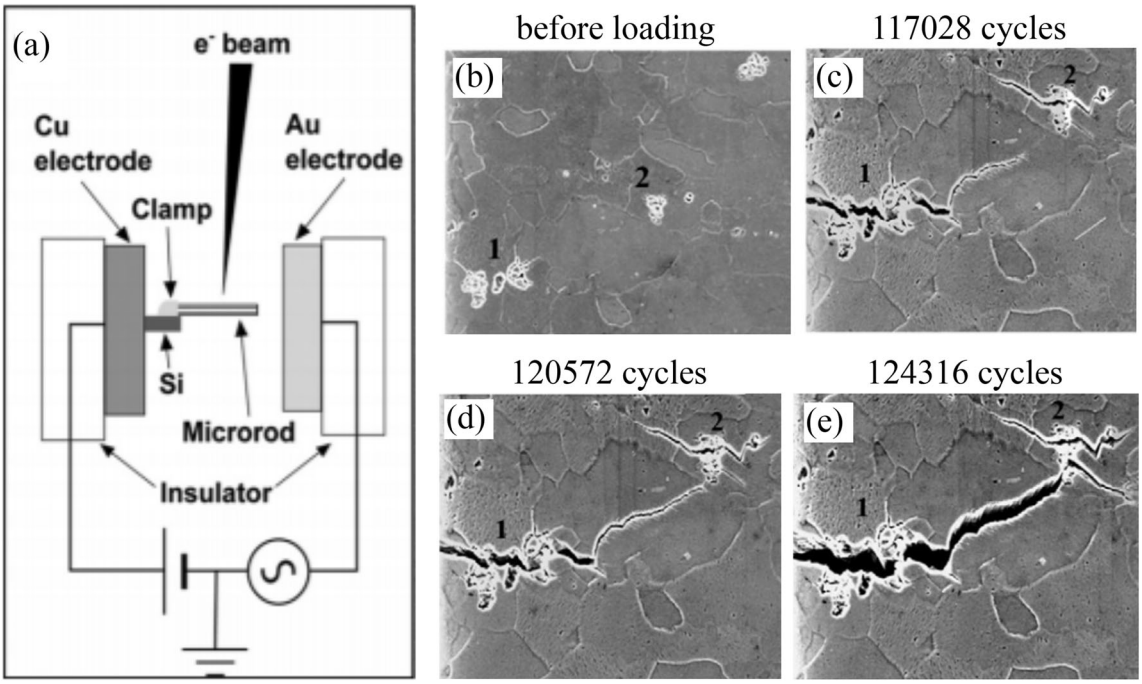

Fig. 8. Young's modulus measurements using IET methods inside SEM. (a) Experimental setup for in situ scanning electron microscopy mechanical resonance measurements. Reprinted with permission from Ref. 34. (b–e) Micrographs for evolution of the main crack under different loading cycles. Reprinted with permission from Ref. 38.

plasmon energy also needs to be determined pixel-by-pixel, as shown in Fig. 9b. Once such an image containing the shift in the plasmon energies in the AL matrix is generated, then the much sought after Y_m map can be generated, like the one shown in Fig. 9d, after the application of Eq. 6. This is how the Y_m maps are generated with the application of Eq. 6 in a pixel-by-pixel manner in the acquired STEM-EELS datasets. This type of Y_m mapping in the dark field STEM mode has been completed by Khushaim and co-workers.[39] Figure 9 describes the complete methodology and data generation steps. One of the biggest advantages of applying STEM-EELS for the determination of mechanical properties is the simultaneous enhancement in the spatial resolutions for both the images and the Y_m. A typical resolution of better than one nanometer for the image and about a couple of nanometers for the Y_m has been demonstrated.

DETERMINATION OF STRAINS

Direct Methods

In many applications of metals in the field of mechanical engineering, loads are applied in a dynamic or impulsive manner which means that the strain rate $\dot{\varepsilon}_R$ can be changed dramatically over time while conducting the experiments. That is why all the components must be designed to operate on a wide range of strain rates. Conventional mechanical tests are generally capable of providing the strain rates up to $10^3 s^-1$. Furthermore, an appropriate set of experimental data needs to be collected and then a corresponding elastic–plastic constitutive model also needs to be chosen to achieve reliable results from the simulations. The engineering as well as the true stress–strain curves, describing the strain hardening behavior up to large strain rates, are the fundamental information among the elastic–plastic parameters. In the present research, the static (strain rate about $10^-3 s^-1$) and dynamic (strain rate about $5 \times 10^2 s^-1$) mechanical behavior of AA6016 alloy sheets has been determined in T4 and T6 temper conditions.[40] The data were fitted by using the Swift–Voce hardening model. The data are presented in Fig. 10, in which a and b contain optical images of the specimens after necking has taken place after applying the load, whereas Fig. 10c shows the engineering stress versus engineering strain curves for each case. It should be noted that the included specimens were of three types, i.e., the first was cut in the transverse, the second in longitudinal, and the third in the diagonal plate rolling direction. The comparison of the tensile curves among the three tested directions show a substantial overlap, thus evidencing a nearly isotropic behavior. The correlation of the microstructure and property is carried by acquiring the images with an optical microscope. Therefore, only the morphology (or shape) changes can be determined from the images in Fig. 10.

The spatial resolution of the images can be significantly improved if the same type of tensile testing fits the existing SEM and even TEM stages. In this way, these techniques are labeled as in situ SEM and in situ TEM for the mechanical testing of

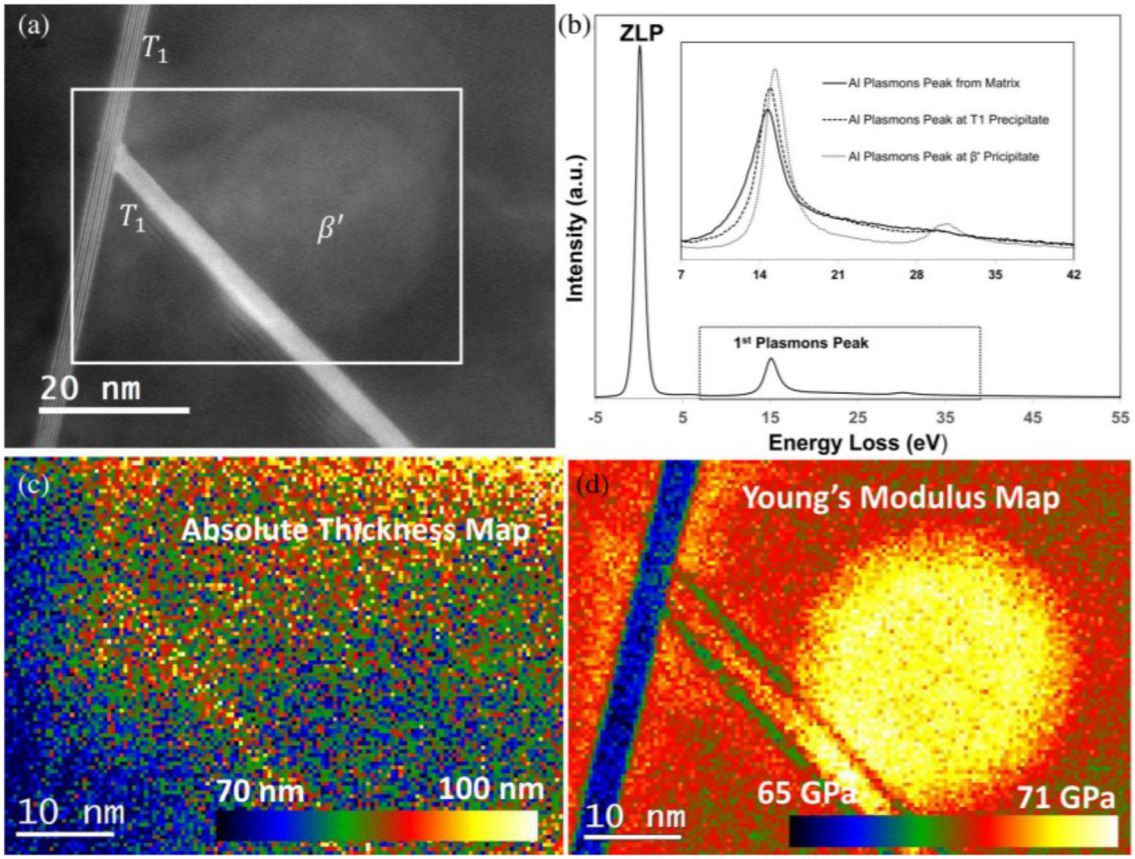

Fig. 9. Mapping of Y_m in the AA2195 alloy using STEM-EELS.(a) HAADF-STEM image containing T_1 platelet precipitate, β spherical precipitate, and Al matrix. (b) EELS spectrum from an Al matrix region. *Inset* plot having overlaid Al plasmon peaks from Al matrix alone, and the matrix having T_1 and β precipitates. (c) Absolute thickness map acquired for Al matrix. (d) Mapping of Y_m by applying NLLS to STEM-EELS. Reproduced under the terms of the Creative Commons CC-BY license (http://creativecommons.org/licenses/by/4.0).[39]

metals. They enable making the observations of a complete tensile test during the experiment, along with accurate stress–strain curves. The in situ SEM and TEM allow the applying of the mechanical characterization of freestanding thin films with thickness of the orders of nanometers to micrometers, and under uniaxial tension. The material under test is first patterned on the silicon substrate using lithography. It is then released from the substrate. A force sensor is also fabricated with the specimen and the whole tensile-testing setup can easily fit existing SEM and TEM stages. Hague and co-workers fabricated a 200-nm -thick, 23.5-μ*m*-wide, and 185-μ*m*-long freestanding Al specimen and tested it in an environmental SEM chamber.[41] An SEM image of the tensile test chip and the SEM-ready experimental setup are shown in Fig. 11(a and b, respectively. During the test, the specimen was continuously monitored in the SEM as shown in Fig. 11c-h, depicting a few frames that were captured in the video. Such experiments are rapidly growing as they offer a cheap and easily fabricated platform to test a variety of nanoscale samples. Similarly, mechanical testing inside the TEM chamber with atomic resolution has been reported in.[42] The authors presented a uniaxial tensile test setup that co-fabricated nanosized freestanding specimens with force and displacement sensors, which can also be accommodated by a TEM straining stage. Overall, it is evident that both SEM and TEM imaging analyses provide higher spatial resolution than an optical microscope, i.e., nanometers to deep sub-nanometers. Therefore, the quality of observing the changes in the microstructure of samples is dramatically enhanced during applied loads. As a consequence, more fundamental structure-to-property relationships can be established using in situ SEM and/or in-situ TEM.

Tensile testing to measure ε_T in the in situ TEM can be utilized at the highest spatial resolution possible.[43] The experimental setup along with ε_T results on Al alloys are presented in Fig. 12. The alloy specimen is prepared using a focused ion beam and strained by applying tensile load. This leads to the generation of applied load versus ε_T plots shown in Fig. 12e. The fitting of the plot and then calculation of the slope leads to the calculation of Y_m of the alloys. In addition to measuring the mechanical ε_T, the in situ TEM is also used to image the microstructure of the alloys at atomic scales, therefore, allowing the establishment of SPCs for ε_T at the nanoscale.

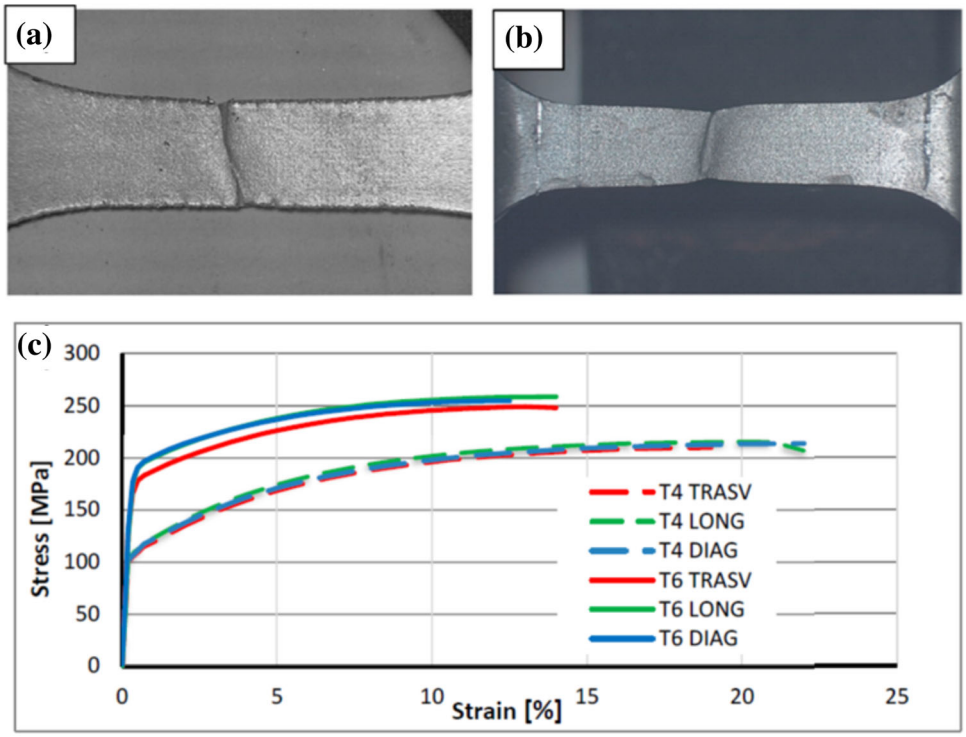

Fig. 10. Samples at the end of the static (a) and dynamic (b) tests. (c) Representative engineering stress–strain static curves of tensile specimens in T4 and T6 temper conditions. Reproduced under the terms of the Creative Commons CC-BY license (http://creativecommons.org/licenses/by/4.0).[40]

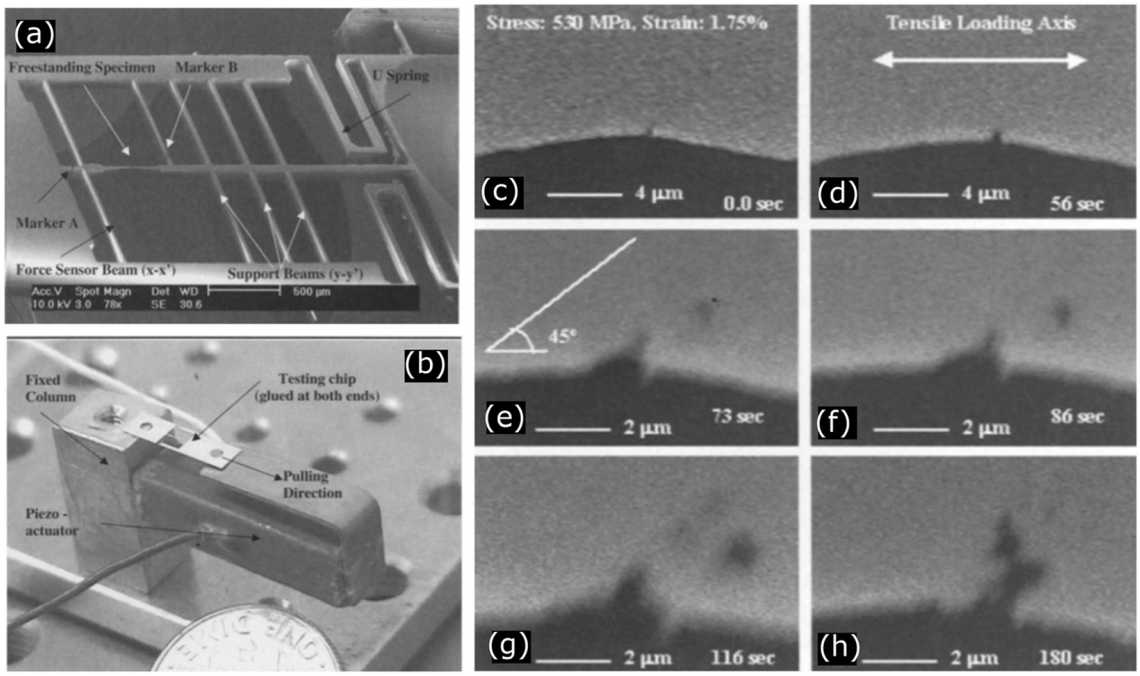

Fig. 11. (a) SEM image of the tensile test chip, (b) SEM-ready experimental setup. Crack propagation: (c) crack visible for the first time (0.0 s), (d) after 56 s, (e) zoomed view after 73 s, showing void coalescence ahead of the crack front at the 45° angle, (f) after 86 s, showing more nuclei of void growth and coalescence, (g) after 116 s, and (h) crack front is large enough to grow normal to the tensile axis. Reprinted with permission from Ref. 41.

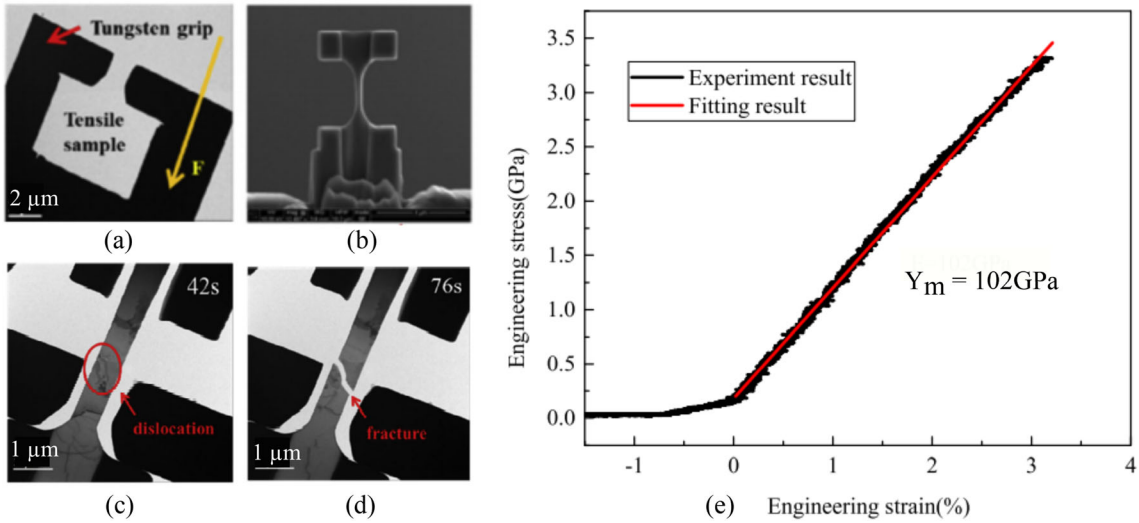

Fig. 12. Tensile testing of Al alloys with in situ TEM. (a, b) Tensile specimen, (c, d) evolution of fracture process during in situ TEM tensile testing, (e) stress–strain curve from the in situ TEM tensile testing. Reprinted with permission from Ref. 43.

Indirect Methods

The strain measurements using indirect methods give rise to the determination of structural or residual strains. Therefore, also combining these with Y_m results in the determination of residual stresses. Interestingly, residual strains are generally determined using techniques that give the results in the nanometer range. This is because, unlike tensile strains, the residual strains are closely linked with the microstructure of alloys. The structural characterization at the nanoscale is often enough to determine the residual strains. This is carried out using indirect and non-destructive methods such as electron backscattered diffraction (EBSD) and nanobeam diffraction (NBD) having residual strain maps with nanometer-range spatial resolutions. EBSD and NBD setups used in a SEM and a TEM for strain mapping of smaller areas using forward scattered diffraction space are given in Fig. 13. EBSD is a powerful tool which is more site-specific, utilizing the electrons with a wavelength much smaller than that of x-rays. This technique has been widely accepted due to its potential to quantify residual strains at the nanoscale. Both elastic and plastic strain effects can be clearly observed in EBSD patterns. It also provides microstructural features, grain boundary orientation, grain size and shape, and other material characteristics, allowing characterization at the sub-10 nm scale. However, to obtain high-quality EBSD patterns, careful sample preparation is highly required as EBSD is a surface-sensitive technique. A detailed review of strain analysis using the EBSD tool has been reported in Refs. 44–46. Furthermore, dislocations due to the growth of grains,[47] mechanical properties of Al 2024 after severe plastic deformation, and non-isothermal annealing,[48] the microstructures of laser-deposited Al 2024 samples[49] and the texture of various burnished subsurface layers of Al alloys[50] have all been explored by using the EBSD tool.

As mentioned above, NBD is a TEM-based technique that also allows the determining of residual strains. In a conventional TEM, it allows the determining of the strains in materials with a spatial resolution that can be either close or higher than EBSD. However, the field-of-view (FOV) of the acquired datasets is significantly smaller for the case of NBD than EBSD, as can be confirmed by looking at the ranges of EBSD and NBD images in Fig. 13. The crystal structure and strain analysis with the help of the NBD tool has been reported in Ref. 51, obtaining diffraction patterns from a 1- to 10-nm region of the specimen. However, to date, TEM is a most efficient investigation tool that permits crystal orientation, and lattice parameter and quantitative strain measurements, in nanograin structures with significant resolution. A nanoscale strain characterization in the Al 2024 alloy was realized in Ref. 52 by using TEM-based NBD technology. Generally, the EBSD setup is used in SEM for strain mapping of large areas using backscattered diffraction space. Overall, by using these techniques, it is possible to establish between the residual strains and microstructure of materials.

The determination of residual strain fields in the Al matrix surrounding the precipitates is often desired but requires higher spatial resolution than either the EBSD or NBD techniques provide. This task can also be carried out in TEM by applying elaborate image processing routines on the acquired high-resolution TEM or high-resolution STEM (HRSTEM) images of the alloys. One of most commonly used image processing techniques is called geometrical phase analysis (GPA) and it basically allows the determining f the atomic displacements in the acquired images with respect to reference regions that ultimately are represented

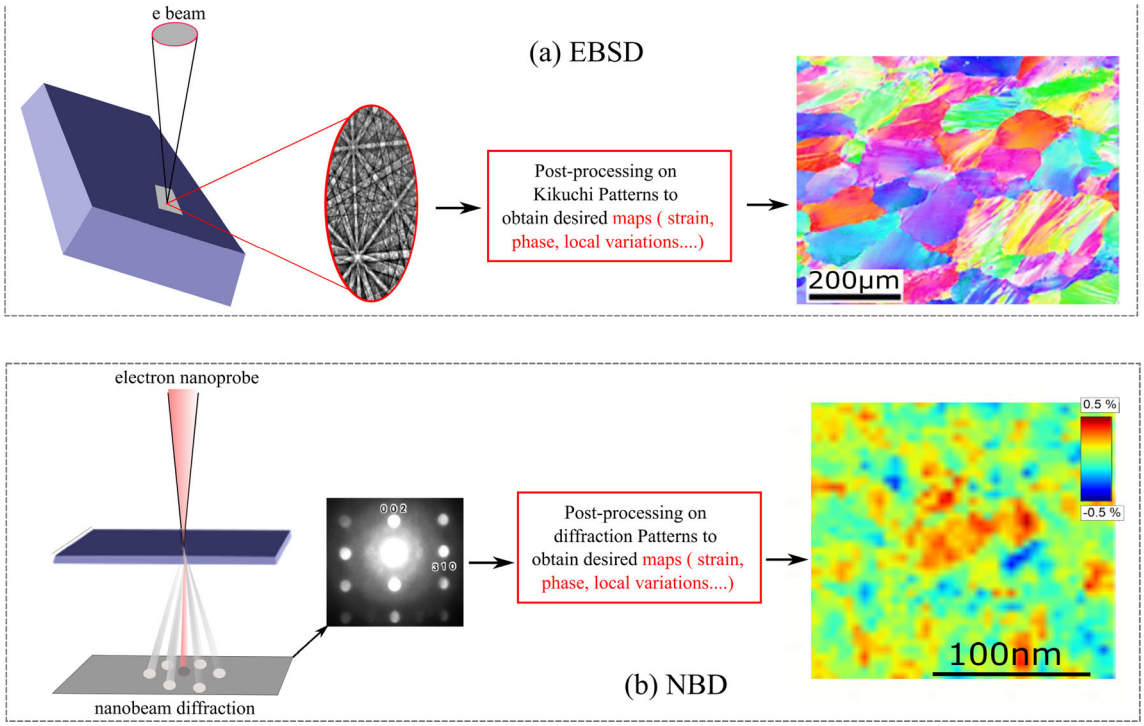

Fig. 13. (a) Schematic of EBSD setup in SEM for strain mapping of large areas using backscattered diffraction space. (b) Schematic of NBD setup in TEM for strain mapping of smaller areas using forward scattered diffraction space.

in the form strain fields.[11,53,54] Its algorithm is based on the implication of atomic resolution on the Fourier space technique.[11] Measurements of strain fields with the GPA technique yield a 0.003-nm sensitivity and has been applied to a wide variety of materials including metallic materials.[54]

For the case of Al alloy materials, the calculation procedures for the strain fields around the observed hardening precipitates require (1) HRSTEM images of the precipitates in Al matrix, (2) calculating the fast Fourier transformation (FFT) of the obtained images, (3) selecting different diffraction spots along different lattice directions, (4) obtaining the inverse FFT of the obtained images, (5) calculating the geometric phase image by using the relationship between the phase of the local Fourier component (P_g)® and the component of the displacement field ($u(r)$); this relationship can be expressed by ($P_g(r) = -2\pi g u)$)®, where g is a reciprocal lattice vector,[11] (6) calculating the displacement field using the relationship for two independent phase images P_{g1})® and P_{g2})®; in this case, the two-dimensional displacement field can be calculated by Eq. (7):

$$\begin{pmatrix} u_x \\ u_y \end{pmatrix} = \frac{-1}{2\pi} \begin{pmatrix} g_{1x} & g_{1y} \\ g_{2x} & g_{2y} \end{pmatrix}^{-1} \begin{pmatrix} P_{g1} \\ P_{g2} \end{pmatrix} \tag{7}$$

where g_x, g_y are two parameters of g in the reciprocal space, and u_x, u_y are atomic displacement fields in normal coordinate, and (7) obtaining the strain field by differentiating the displacement field as shown by Eq. 8:

$$\varepsilon_{xx} = \frac{\partial u_X}{\partial x}, \quad \varepsilon_{yy} = \frac{\partial u_y}{\partial y}, \quad \varepsilon_{xy} = \frac{1}{2}\left(\frac{\partial u_x}{\partial x} + \frac{\partial u_y}{\partial y}\right) \tag{8}$$

Based on above theoretical framework, the experimental results on Al2024 alloys are shown in Fig. 14.[55] In this work, the authors applied the HRSTEM technique to investigate the sequence of precipitate formation in the alloy. GPA was also applied on the corresponding HRSTEM images to map the residual strain field in the Al matrix surrounding the precipitates. It can be confirmed from the results that HRSTEM in conjunction with GPA is capable of measuring the residual strains at high spatial resolution as well as the sensitivity that can be directly correlated with the microstructure of the precipitate and alloys.

FUTURE OUTLOOK

In recent years, efforts have been made to combine microstructure imaging and property measuring techniques. This has led to the acquiring of different types of datasets in a simultaneous manner from the same regions of alloys. In this way, the acquired results can be utilized to establish the correlated SPCs in an improved way. One way or another, improvements have been made to acquire

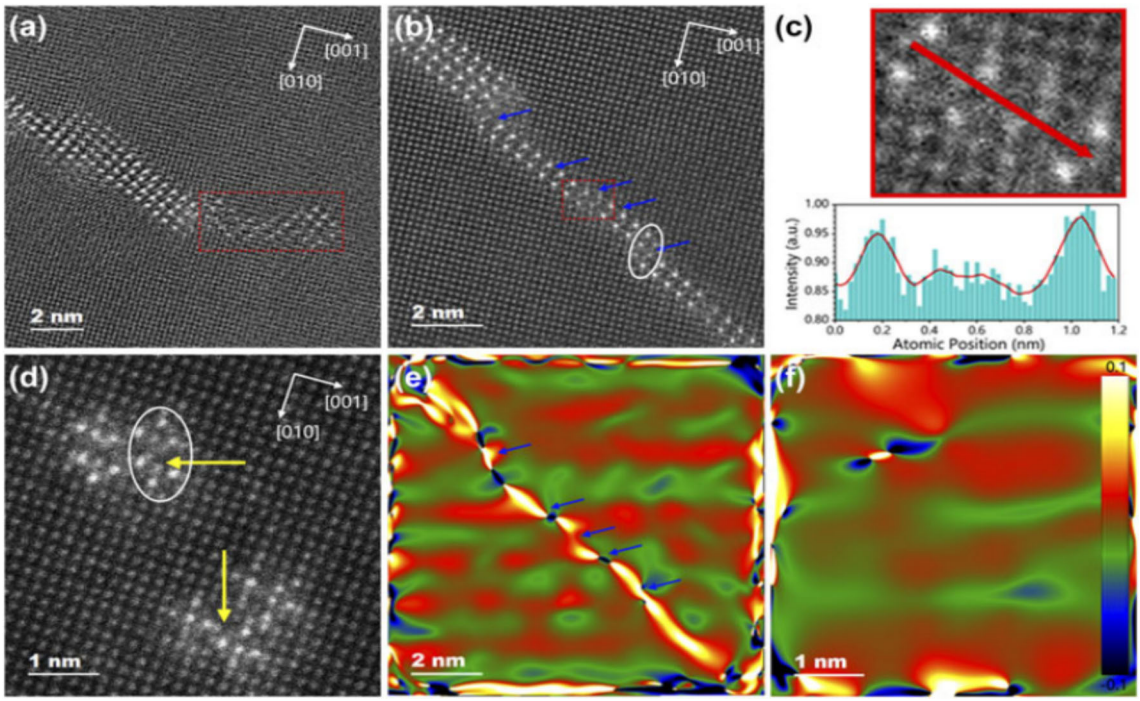

Fig. 14. STEM and GPA characterization results of a specimen with 2-h ageing treatment. (a) Layered *S* phase structure with segregation at the end, (b) single- and double-layered structure with step-shaped variation, (c) magnified image of *red dashed square* in (b) and line plot of image intensity along the *arrow*, and (d) morphology and atomic structure of solute segregation and co-cluster. The projection direction of the four STEM images is parallel to [100]Al; (e) and (f) are the GPA measurement results corresponding to (b) and (d), respectively. *Blue arrows* in (e) represent the positions of defects. *Bar* in (f) is the GPA intensity with a relative value from −0.1 to 0.1. Reprinted with permission from Ref. 55 (Color figure online).

higher quality data from pretty much all of the techniques mentioned above. However, the advancements made for the cases of TEM and APT are particularly noteworthy. Regarding TEM, the so-called 4DSTEM technique allows the combining of various TEM based techniques into a single technique, and hence has become a promising way of determining various material properties including residual strains and elastic modulus. 4DSTEM refers to recording 2D images of a converged electron beam over a 2D grid of beam positions. The resulting datasets are 4D, hence the term 4DSTEM. In other words, all forms of scattering measurements that are present in 2D images of a STEM probe are recorded. This is done either in real or diffraction space for a 2D grid of beam positions. The complete history, name conventions, and some recent developments on the 4DSTEM technique can be found from.[56] One of the weaknesses of conventional STEM imaging; namely that the bright and dark field detectors must be physically positioned at some angle from the optical axis. Moreover, those detectors cannot be changed relative to each other during the measurements. Under this scheme, after carrying out a conventional STEM measurement, electrons within the scattering range are grouped together and can no longer be further separated by the scattering angle. The illustration of this fact is mentioned in "Indirect Methods" section for the case of NBD. The 4DSTEM technique allows this weakness of NBD to be overcome for determining the strain of materials simultaneously at a high spatial resolution and signal sensitivity. It allows the production of strain maps by providing "virtual" detectors that can be added (or subtracted) to some subset of the pixels in the diffraction patterns at each probe location.

The application of the 4DSTEM technique for strain measurements has an inherent trade-off between the resolutions in real space and reciprocal space. A larger convergence angle will generate a smaller probe, giving better resolution in real space. However, this will also decrease the strain measurement precision due to the overlapping of the diffracting peaks. To circumvent this problem, the convergence angle can be decreased, leading to an increase of the STEM probe size in real space. A 4DSTEM measurement under these conditions will have a somewhat lower spatial resolution but certainly an improved strain precision. Relatively, a smaller FOV is generally a limitation to the advancement of strain measurements using TEM modalities. 4DSTEM offers a solution to this by using millisecond readout times with direct electron detectors. In this way, the FOV can be increased, as demonstrated by Müller and co-workers.[57] The data acquired under this scheme show that 4DSTEM strain measurements present several advantages

over strain measurements made with NBD.[56] For instance, it was demonstrated that the 4DSTEM enhances the FOV equal to EBSD's FOV but at a higher spatial resolution. Second, the heterogeneity could also be addressed by acquiring the 4DSTEM data under precession electron diffraction (PED) conditions for various types of materials, including single-crystalline semiconductor multilayers and poly-crystalline materials. Third, Ebner and co-workers[58] showed that it was possible to measure this structural variation in metallic glasses. By the same token, Austl. and co-workers and Redman and co-workers utilized the 4DSTEM technique to measure residual strains in samples with large FOV and poly-crystalline materials, respectively.[59,60] Using a method that combined PED with 4DSTEM experiments and performing the subsequent experiments with a fast detector, Gammer and co-workers[61] were able to map the strain distribution in metallic glass samples that were machined into a dog-bone geometry for in situ mechanical testing. The acquired results showed an intermediate time step where the sample was under mechanical load, while the mean image data revealed the characteristic "amorphous ring" which was a good fit for every probe position to determine the relative strain maps, referenced to the unloaded sample. With all these advancements within the reach, it is just a matter of time before the results of the strain measurements of Al alloys using 4DSTEM will appear.

Another aspect of current efforts includes the advancements made in the field of 4DSTEM data processing. Almost every study described in this section uses computational imaging in some capacity. The digital recording of microscopy images and diffraction patterns has quickly replaced the previously used photographic film technology, because it made it easy to use computers to analyze the acquired data. There are several packages that are currently being developed for 4DSTEM data analysis. These include HyperSpy, pyXem, LiberTEM, Pycroscopy, and py4DSTEM. Because so many of the 4DSTEM methods and technologies mentioned here are being actively developed, it is expected that the software landscape will change considerably and will also be applied to the analysis of 4DSTEM datasets from metals and their alloys.

In the context of using different techniques and correlating them, a well-established approach that allows a direct comparison of APT and small-angle (x-ray) scattering (SAXS) performed on the same material was presented in Ref. 62. Comparing between techniques was carried out for a range of Al alloys. By this approach, an accurate analyzing property-enhancing particle in the nanosize range and below would be possible. As has been frequently highlighted, APT has progressively become prominent as a tool for analyzing the composition of microstructural features that are precipitate features in the nanometer-size range and below.[63,64] This is particularly true for solute clusters.[65] However, there are still debates as to how to define a solute cluster and whether it is possible to distinguish between a random fluctuation and a "real" cluster. Additionally, the question of the effective spatial resolution for APT in the analysis of particles has never been addressed. To address this question, De Geuser and co-workers[62] reported on the results obtained by using SAXS and APT techniques performed on the same material. SAXS allows the detection of compositional fluctuations on the smallest scale and does not suffer from the same artefacts as APT. It has been demonstrated that the effective spatial resolution of APT in the context of the metrology of small objects is worse than often reported, which will particularly impact the measurement of solute clusters and small precipitates. Thus, when approaching 1 nm in radius, the measured values of the size and composition of particles by APT should be considered highly questionable. Possible routes for more reliable results on very small objects can be obtained by using statistical methods such as radial distribution functions-based analyses and including the effect of the point spread function in the interpretation of these analyses.

SUMMARY AND DISCUSSION

In this section, the qualitative problem statement, presented by the schematic shown in Fig. 1, is represented in more substantive and quantitative shape. This is presented in Fig. 15 and is completed by giving an overall summary of the quality on the established SPCs by performing correlations between the measured mechanical properties as well as the determined microstructure of the alloys. It can be seen from Fig. 15 that the SPCs can be divided into three regions based on length scales, namely macro-, transition, and nanoscales. Strictly speaking, these scales work for the microstructure but, qualitatively, the spatial resolution of the mechanical properties also increases as we move from macro- to nanoscales. It is also abundantly clear that, for either the "direct" or "indirect" categories, a combination of minimum two or three techniques is required to established the SPCs at a specific length scale. For instance, for the direct category and at macroscale, the establishment of SPCs requires a combination of three techniques, namely NI, tensile testing (TS), and optical microscopy (OM) for Y_m, tensile strain, and microstructure, respectively. Several conclusions can be made from the schematic given in Fig. 15.

- NI is used to determine Y_m under direct category (or under applied load conditions) at bulk scales.[19] Similarly, under the same category and scales, the ε_T is determined using the bulk tensile testing method. In either case, the commensurate imaging of both NI-investigated and tensile tested regions is performed with OM. This is how the SPCs can be established by

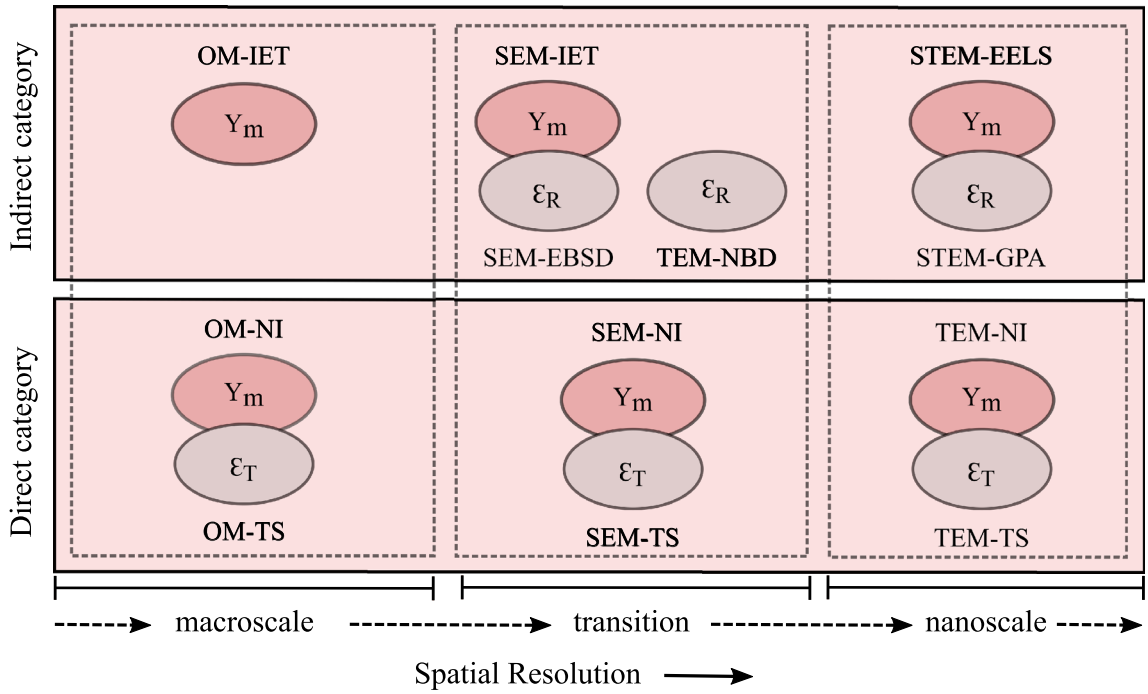

Fig. 15. Summary of the techniques capable of providing microstructure–property correlations for direct and indirect categories in different length scales. Each combination represents a set of techniques that provide information on the Y_m, ε_T or ε_R, and microstructure. Each combination of microstructure measuring technique and mechanical property determining technique is presented in microstructure technique-mechanical property technique manner. This combination is written above the *oval* containing Y_m property and whereas below the *ovals* containing ε_T and ε_R properties.

analyzing the data presented in Figs. 4 and 10. It is to be noted that the OM-determined evolution in the microstructure of the alloys is practically reduced to morphological changes recorded under compressive and tensile load conditions. It is worth noting that only the microstructure of the alloys is recorded in images (or 2D maps), whereas both mechanical quantities are measured in the form of plots, which means that the determined Y_m will be a scalar number.

– For the case of the indirect category and bulk scales, the situation is quite different. First, strain without the application of tensile load will reduce to ε_R and there is no technique that is capable of providing data on residual strain under indirect conditions. Therefore, only the Y_m under these scales and category can be determined. This is done using the technique of IET. The results presented in Fig. 7 show that IET provides the Y_m in the form of a plot, while the microstructure is determined using OM. Due to the inherent technique limitations of OM and IET, the acquired results possess micron-scale spatial resolutions.
– At the transition length scales, the established SPCs have spatial resolutions in deep submicron scales. Such resolutions can be in the microstructure and/or the mechanical properties. For the case of the direct category, the experiments of applying both compressive (NI) and tensile (TS) loads are moved to SEM, as shown in the Figs. 5 and 11, respectively. By doing so, the spatial resolution of the microstructure improved to a few nanometers. Furthermore, the spatial resolutions also improved significantly in the data acquired for both Y_m and ε_T due to a reduction in the size of specimens needed to investigated inside SEM. Even having higher resolutions of the microstructure (i.e., down to individual grains), the data on the mechanical properties is still acquired in the form of plots. Consequently, the established SPCs under this category and length scales will have higher spatial resolutions but smaller FOVs.
– Next, at the same transition scales but for the indirect category, the IET experiments can be carried out inside SEM to improve the resolution of the microstructure data (Fig. 8). Thus, the established SPR for Y_m under category will have similar characteristics as the direct category in the same length scales. However, in the indirect category ε_R is measured by using the EBSD setup in SEM, as shown in Fig. 13. EBSD allows the generating of maps or 2D plots of ε_R with a range of tens of microns as opposed to 1D plots by using TS. The typical spatial resolution of the generated 2D maps of ε_R is in the range of 3–10 nm per pixel which is close to the spatial resolution in the images of the corresponding microstructure. To have an enhanced spatial

resolution (i.e., 1–3 nm) in both microstructure and ε_R, but at a smaller FOV, the experiments can be performed in TEM by setting it in NBD mode (Fig. 13).

– For the direct category, the highest spatial resolution, i.e., one nanometer or below, in both the microstructure and property is possible by performing the NI and tensile experiments inside the TEM. The method allows imaging the microstructure near atomic resolutions during the indentation and/or tensile experiments, and the results from these techniques are presented in Figs. 6 and 12, respectively. The determined Y_m and ε_T are scalar numbers determined from the 1D plots under schemes mentioned in "The Direct Methods" and "Direct Methods" sections, respectively. The independent determination of both properties results in the estimation of applied stress in the alloys.
– For the indirect category and the highest spatial resolutions, the determination of both microstructure and property are possible by carrying out HRSTEM imaging and STEM-EELS experiments, respectively. The methodology for determining Y_m is presented in Fig. 9. It is to be noted, using STEM-EELS, that the Y_m results can be presented in 2D plots or maps. GPA on HRSTEM enables the generating of ε_R maps in addition to providing the high-resolution details of the microstructure (Fig. 14). It is clear that the combination of STEM-EELS and HRSTEM-GPA is unique in the sense that it is the only way to provide 2D plots (or maps) for both strain and Young's modulus. As mentioned earlier, the Y_m at the nanoscale is different than at the macroscale for the materials Therefore, this combination gives the opportunity of determining a size-dependent Y_m for the Al alloys. Furthermore, finding out Y_m this way will help to investigate whether other mechanical properties of the alloys increase, decrease, or remain constant, as has been observed for other materials.[66–68] As a result, it will become possible to find out whether Hooke's law and Euler–Bernoulli theory for the elastic behavior of materials are sufficient to explain the properties of Al alloys at the nanoscale or the dependence of Y_m on the size must be included.[69]

CONCLUSION

1. Overall, the schematic of a general SPC presented in Fig. 1 has been given a quantitative representation in Fig. 15. This turned out to be a combination of techniques that work for different categories of mechanical properties and microstructure. Moreover, a specific combination is valid for a given length scale of the three mentioned here, i.e., macro-, transition, and nanoscales.
2. It was thus demonstrated that the combination of a microstructure measuring techniques and a particular property determining technique dictate the quality of established SPCs. The nature and validity of the established SPCs depends on the size in the same way as the mechanical properties and microstructure. It can also be concluded that NI belongs to the direct category technique which allows the determining of Y_m independently at different scales.
3. Similarly, tensile testing (TS) enables the measuring of the tensile strains or ε_T at different scales for the direct category. Under this testing scheme, the applied stresses can be linked to the independently measured Y_m and ε_T. It is to be noted that no combination of these techniques gives either Y_m or ε_T in the form of 2D plots or maps. On the other hand, the microstructure at the same length scale can be recorded in 2D plots or images. The spatial resolution of the acquired images increases with decreasing the scales because the imaging technique is changed for each case.
4. For the indirect category, there is no technique that allows measuring the residual strain of ε_R at bulk scales. In this category, only IET can be employed to measure Y_m at these scales. However. the spatial resolution of the microstructure recorded images will be limited by the optical microscopy which can be enhanced to the nanometer scale by performing IET experiments in SEM.
5. The EBSD datasets acquired in SEM allow the determining of the ε_R at transition scales, i.e. between the bulk- and nanoscales. The generated strain data are in the form of 2D strain maps with a spatial resolution of about 5 nm. In the same transition scales, the spatial resolution of ε_R maps can be enhanced a little by acquiring the NBD datasets in the STEM of a TEM.
6. Clearly, the highest resolution containing ε_R maps can only be generated by applying GPA on the acquired HRSTEM images of the alloys.
7. By the same token, the STEM-EELS is the only indirect category technique that allows the determining of Y_m at the nanoscale with nanometer spatial resolution. Furthermore, STEM-EELS is the only technique among all the techniques available in either direct on indirect categories that can give the Y_m in the form of 2D plots or maps.
8. It was contended that in the direct category both Y_m and ε_T are measured as scalar numbers by carrying out NI and TS experiments in the in situ TEM, whereas, for the indirect category, Y_m and ε_T are measured as two plots by carrying out STEM-EELS experiments and

STEM-GPA data processing. 4DSTEM can be developed to apply on small grain sizes or amorphous Al alloys.

9. The application of a certain technique from either category will depend on the specific information required. For instance, residual stress is a kind of internal deformation coordination of materials, which is caused by constraints or non-uniform deformations, and is an important factor for evaluating deformation materials. Similarly, tensile strain-based techniques will be chosen if the requirement if to measure the mechanical strength of alloys.
10. In the end, it is important to note that no single technique can do it all when it come to correlating the mechanical properties with the microstructure of the alloys. For example, NI experiments combined with in situ TEM present the best solution for studying the dislocation motions under applied loads. Similarly, STEM-EELS offers the best option to determine the Young's moduli and residual strain in the metal alloys at the nano scale.

FUNDING

The authors extend their appreciation to Abu Dhabi Department of Education and Knowledge (ADEK) for partially funding this research work under the Project ID: AARE-131 2019, to Khalifa University's Faculty Startup (FSU) program for partially funding this research work under the project ID: FSU-2020-04, and to the Deputy ship for Research & Innovation, Ministry of Education in Saudi Arabia for partially funding this research work the project number (442/144). Also, the authors would like to extend their appreciation to Taibah University for its supervision support.

CONFLICT OF INTEREST

The authors show no conflict of interest.

REFERENCES

1. A.C. Reardon, *Metallurgy for the Non-Metallurgist*, 2nd edn. (Ohio: ASM International, 1995).
2. M. Fleischer, *J. Chem. Edu.*, 31(9), 446 (1954).
3. P.A. Frey and George H. Reed, *ACS Chem. Biol.*, 7(9), 1477 (2012).
4. G.E. Totten and D.S. MacKenzie (eds.), *Handbook of Aluminum, Physical Metallurgy and Processes* (Boca Raton: CRC, 2003).
5. I.J. Polmear, Metallurgy of the light metals, in *Light Alloys*, 3rd edn. (London: Edward Arnold, 1995).
6. E.A. Starke and J.T. Staley Jr., *Progr. Aerosp. Sci.*, 32, 131 (1996).
7. E.A. Starke, T.H. Sanders, and I.G. Palmer, *JOM*,33, 24 (1981).
8. K.V. Jata and E.A. Starke, *Metall. Trans. A*, 17, 1011 (1986).
9. E.A. Starke Jr. and T.H. Sanders Jr., *Met. Soc. AIME* (1984).
10. Y.J. Lee and K. Jiraga, *J. Mater. Res.*, 14, 384 (1999).
11. M.J. Hÿtch, E. Snoeck, and R. Kilaas, *Ultramicroscopy*, 74, 131 (1998).
12. A. M. Abazari, S. Mohsen Safavi, G. Rezazadeh, and L. Guillermo Villanueva, Size Effects on Mechanical Properties of Micro/Nano Structures, arxiv:1508.01322, (2015).
13. M.K. Miller and A.P. Tomography, *Analysis at the Atomic Level*. (2000).
14. B. Gault, M.P. Moody, J.M. Cairney, and S.P. Ringer, *Atom Probe Microscopy*, vol. 160 (Cham: Springer, 2012).
15. M. S. Khushaim, *Encyclopedia of Aluminum and Its Alloys*, Chapter: Precipitation in AA2195 by Atom Probe Tomography and Transmission Electron Microscopy, (Boca Raton: CRC (2018). https://doi.org/10.1201/9781351045636-140000220.
16. I. Polmear, *Light Alloys: From Traditional Alloys to Nanocrystals* (Amsterdam: Elsevier, 2005).
17. S. Wenner, L. Jones, C.D. Marioara, and R. Holmestad, *Micron*, 96, 103 (2017).
18. S.J. Pennycook and C. Colliex, *MRS Bull*, 37, 13 (2012)..
19. L. Qian, M. Li, Z. Zhou, H. Yang, and X. Shi, *Surface Coat. Technol*, 195, 264 (2005).
20. C.H. Hsueh, S. Schmauder, C.S. Chen, K.K. Chawla, N. Chawla, W. Chen, and Y. Kagawa, (eds.), *Handbook of Mechanics of Materials* (Cham: Springer, 2019), pp. 760–792.
21. H. Yu, J.B. Adams, and L.G. Hector Jr., *Modell. Simul. Mater. Sci. Eng.*, 10, 319 (2002).
22. V. Králík and J. Němček, *Mater. Sci. Eng. A*, 618, 118 (2014).
23. C.-L. Chen, A. Richter, and R.C. Thomson, *Intermetallics*, 17, 634 (2009).
24. M. Dao, N.V. Chollacoop, K.J. Van Vliet, T.A. Venkatesh, and S. Suresh, *Acta Mater.*, 49, 3899 (2001).
25. N. Ogasawara, N. Chiba, and X. Chen, *Scr. Mater.*, 54, 65 (2006).
26. E. Harvey, L. Ladani, and M. Weaver, *Mech. Mater.*, 52, 1 (2012).
27. C.A. Charitidis, D.A. Dragatogiannis, E.P. Koumoulos, and I.A. Kartsonakis, *Mater. Sci. Eng. A*, 540, 226 (2012).
28. L. Shen, W.C.D. Cheong, Y.L. Foo, and Z. Chen, *Mater. Sci. Eng. A*, 532, 505 (2012).
29. X. Lan, K. Li, F. Wang, S. Yanqing, M. Yang, S. Liu, J. Wang, and D. Yong, *J. Alloys Compd.*, 784, 68 (2019).
30. A. Staszczyk, J. Sawicki, L. Kołodziejczyk, and S. Lipa, *Coatings*, 10, 846 (2020).
31. J.D. Nowak, K.A. Rzepiejewska-Malyska, R.C. Major, O.L. Warren, and J. Michler, *Mater. Today*, 12, 44 (2010).
32. O.L. Warren, Z. Shan, S.A. Syed Asif, E.A. Stach, J.W. Morris Jr., and A.M. Minor, *Mater. Today*, 10, 59 (2007).
33. Ae. Hauert, A. Rossoll, and A. Mortensen, *Compos. Part A*, 40, 524 (2009).
34. J. Bartolomé, P. Hidalgo, D. Maestre, A. Cremades, and J. Piqueras, *Appl. Phys. Lett.*, 104, 161909 (2014).
35. James M. Howe, and V.P. Oleshko, *Microscopy*, 53, 339 (2004).
36. M. Monthioux, F. Soutric, and V. Serin, *Carbon* 35, 1660 (1997).
37. Vladimir P. Oleshko, M. Murayama, and J.M. Howe, *Microsc. Microanal.*, 8, 350 (2002).
38. L. Yan and J. Fan, *Mater. Design*, 110, 592 (2016).
39. Muna S. Khushaim, and D.H. Anjum, *Microsc. Res. Tech.*, 84, 869 (2021).
40. U. Graziano, P. Matteis, S. Ferraris, C. Marcianò, F. D'Aiuto, M.M. Tedesco, and D. De Caro, *Metals*, 10, 242 (2020).
41. H.M. Amanul and M.T.A. Saif, *Exper. Mech.*, 42, 123 (2002).
42. H.M. Amanul and M.T.A. Saif, *J. Mater. Res.*, 20, 1769 (2005).
43. Z. Cai, X. Cui, G. Jin, L. Binwen, D. Zhang, and Z. Zhang, *J. Alloys Compd.*, 708, 380 (2017).
44. A.J. Wilkinson, T.B. Britton, J. Jiang, and P.S. Karamched, *IOP Conf. Series: Mater. Sci. Eng.* 55, 012020 (2014).
45. Stuart I. Wright, M.M. Nowell, and D.P. Field, *Microsc. Microanal.*, 17, 316 (2011).
46. Angus J. Wilkinson, and T.B. Britton, *Mater. Today*, 15, 366 (2012).

47. Salehi Majid Seyed, N. Anjabin, and H.S. Kim, *Microsc. Microanal*. 25, 656 (2019).
48. Moghanaki Saeed Khani and M. Kazeminezhad, *Trans. Nonferr. Metals Soc. China* 27, 1 (2017).
49. T. Gu, B. Chen, C. Tan, and J. Feng, *Opt. Laser Technol*., 112, 140 (2019).
50. J. Zou, H. Luo, Zhiyuan Han, and J. Lv, *Nanosci. Nanotechnol. Lett*., 5, 355 (2013).
51. P. Favia, M. Popovici, G. Eneman, G. Wang, M. Bargallo-Gonzalez, E. Simoen, N. Menou, and H. Bender, *ECS Trans*., 33, 205 (2010).
52. R. Florent, D. Anjum, C. Aubry, G. Haidemenopoulos, H. Kamoutsi, H. Mavros, N. Singh, I. Qattan, G. Das, and S. Patole, *Microsc. Microanal*., 26, 1528 (2020).
53. M.J. Hÿtch and T. Plamann, *Ultramicroscopy*, 87, 199 (2001).
54. C.W. Zhao, Y.M. Xing, C.E. Zhou, and P.C. Bai, *Acta Mater*., 56, 2570 (2008).
55. Chenyang Zhu, K. Lv, and B. Chen, *J. Mater. Res*., 35, 1582 (2020).
56. C. Ophus, *Microsc. Microanal*., 25, 563 (2019).
57. K. Müller, H. Ryll, I. Ordavo, S. Ihle, L. Strüder, K. Volz, J. Zweck, H. Soltau, and A. Rosenauer, *Appl. Phys. Lett*., 101, 212110 (2012).
58. C. Ebner, R. Sarkar, J. Rajagopalan, and C. Rentenberger, *Ultramicroscopy*, 165, 51 (2016).
59. V.B. Ozdol, C. Gammer, X.G. Jin, P. Ercius, C. Ophus, and J. Ciston, and A.M. Minor, *Appl. Phys. Lett*., 106, 253107 (2015).
60. P.F. Rottmann and K.J. Hemker, *Mater. Res. Lett*., 4, 249 (2018).
61. C. Gammer, C. Ophus, T.C. Pekin, J. Eckert, and A.M. Minor, *Appl. Phys. Lett*., 112, 171905 (2018).
62. F. De Geuser and B. Gault, *Acta Mater.*, 15, 406 (2020).
63. E.A. Marquis, M. Bachhav, Y. Chen, Y. Dong, and L.M. Gordon, *Curr. Opin. Solid State Mater. Sci*., 17, 217 (2013).
64. D. Arun, D.E. Perea, J. Liu, L.M. Gordon, and T.J. Prosa, *Int. Mater. Rev*., 63, 68 (2018).
65. D. Phillip, S.S.A. Gerstl, L.T. Stephenson, P.J. Uggowitzer, and S. Pogatscher, *Adv. Eng. Mater*., 20, 1800255 (2018).
66. B. Wu, A. Heidelberg, J.J. Boland, J.E. Sader, X.M. Sun, and Y.D. Li, *Nano Lett*., 6, 468 (2006).
67. B. Alberto, E. Brusa, G. De Pasquale, M.G. Munteanu, and A. Soma, *Analog Integr. Circuits Signal Process*., 63, 477 (2010).
68. N. Takahiro, Y. Isono, and T. Tanaka, *J. Microelectromech. Syst*., 9, 450 (2000).
69. D. Duque, *Eur. J. Phys*., 37(1), 015002 (2015).

Publisher's Note Springer Nature remains neutral with regard to jurisdictional claims in published maps and institutional affiliations.